Int J Thermophys (2009) 30:1823–1837
DOI 10.1007/s10765-009-0685-0

A New Method of Processing Mach–Zehnder Interference Fringe Data in Determination of Diffusion Coefficient

Maogang He · Ying Guo · Qiu Zhong · Ying Zhang

Received: 9 September 2008 / Accepted: 14 November 2009 / Published online: 26 November 2009

Abstract Laser holographic interferometry is the newest method to measure the mass diffusion coefficient and has been widely used in recent years. The processing of interference fringe images is a critical step of getting the final precise experimental results. On the basis of Fourier transformation and phase measurements, a new method of processing Mach–Zehnder interference fringes is introduced in this article. By experimental verification and uncertainty analysis, the accuracy of this method is validated. Mass diffusion coefficients of ethylene glycol dimethyl ether and diethylene glycol dimethyl ether, two new fuel additives in air were measured with the method introduced in this study.

Keywords Mass diffusion coefficient · Laser holographic interferometry · Ethylene glycol dimethyl ether · Diethylene glycol dimethyl ether

1 Introduction

The mass diffusion coefficient introduced by the second Fick's law is a basic thermophysical property in the field of mass transfer, and it represents the fluid's capacity of diffusion [1–3]. It is the basis of the research on the phenomenon of mass diffusion by experiment and by theoretical calculations [4,5]. In recent years, with the development of substitutive fuels, biochemistry, environmental pollution control and isotope separation, theoretical and experimental research on the mass diffusion coefficient have gained more and more attention. Currently, the experimental methods for measuring mass diffusion coefficients mainly include: diaphragm cells [6], Taylor dispersion [7],

M. He (✉) · Y. Guo · Q. Zhong · Y. Zhang
State Key Laboratory of Multiphase Flow in Power Engineering, Xi'an Jiaotong University, 710049 Xi'an, People's Republic of China
e-mail: mghe@mail.xjtu.edu.cn

pulsed-field gradient nuclear magnetic resonance [8], dynamic light scattering [9], and holographic interferometry [10,11]. Compared with other methods, holographic interferometry has the highest accuracy. By different models of interferential light paths, holographic interferometry can be classified according to three types: Gouy, Rayleigh, and Mach–Zehnder interferometry.

Compared with Gouy and Rayleigh holographic interferometry, Mach–Zehnder holographic interferometry has the advantage that its interferential light path is simple, the experimental system is easy to construct, and the change of interference fringes is associated with the physical quantity to be measured. By now, there are several methods of processing Mach–Zehnder interference fringe images such as the method of extracting the centerline of the interference fringe, least-square fitting of the centerline of interference fringes, phase measurement by phase-shift interferometer, etc., the first two methods mentioned above have some accuracy limitations. Although the third method has a high accuracy, its corresponding experimental system needs an additional phase-shifting device. In order to improve the experimental data processing precision and keep the experimental system as simple as possible, in this study, on the base of Fourier transformation and phase measurements, a new method of processing Mach–Zehnder interference fringes is introduced. The new method makes good use of the phase information of the interference fringes and improves the accuracy of the experimental results greatly. The method includes mainly the following steps: wavelet de-noising, frequency-domain wave filtering, object wave reconstruction, and phase unwrapping.

The structure of the article is organized as follows: in Sect. 2, the theory of mass diffusion and the theory of holographic optics are reviewed briefly. In Sect. 3, the new image processing method is introduced step by step. In Sect. 4, the reliability of the new image processing method and the experimental uncertainty are analyzed. In Sect. 5, mass diffusion coefficients of some fuel additives were measured using the new image processing method. Finally, this article will be concluded in Sect. 6.

2 Theory

Figure 1 shows the experimental system used in our laboratory to measure the mass diffusion coefficient of fluids. From this figure, we can see that the laser beam is emitted from He–Ne laser source 1 and is reflected by mirror 2; then the laser beam goes into spatial filter 3 in which it is expanded. The expanded laser beam is collimated by achromatic doublet lens 4 into a parallel laser beam. After that, the parallel laser beam is split into reference beam and object beam by beam splitter 5. The object beam passes through diffusion cell 7 and record the information of diffusion. Finally both the object beam and the reference beam interfere at beam splitter 9 to form the interference fringe which is collected by CCD camera 10 and recorded on computer 11 [12].

Figure 2 shows the diffusion cell used in this study, and it is an improved version of our previous apparatus reported before. In order to make sure the experiment goes on in a stable temperature environment, the diffusion cell is placed in the thermostatic water bath and the thermostatic water is supplied by the thermostatic water system

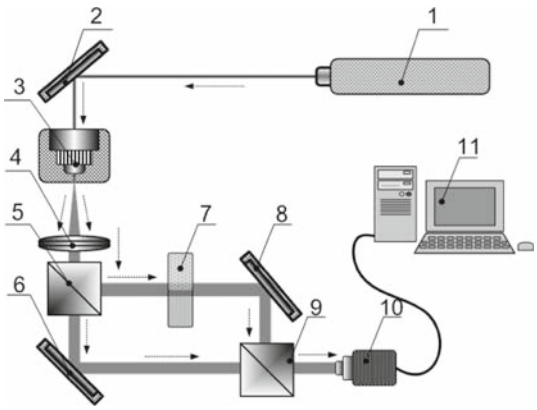

Fig. 1 Experimental system of Mach–Zehnder holographic interferometry: *1* He–Ne Laser; *2*, *6*, *8* mirror; *3* spatial filter; *4* achromatic doublets lens; *5*, *9* beam splitter; *7* diffusion cell; *10* CCD camera; *11* computer

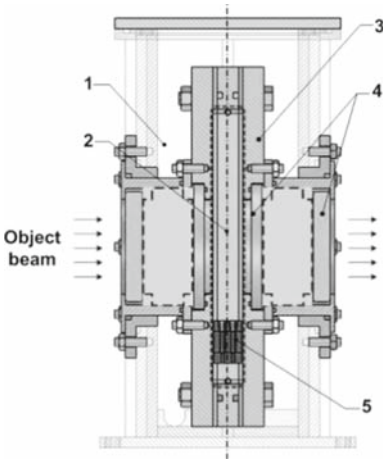

Fig. 2 Diffusion cell system: *1* thermostatic water bath, *2* diffusion zone, *3* diffusion cell, *4* optical glass, *5* honeycomb

(shown in Fig. 3) whose temperature could be controlled from (0 to 80) °C with an uncertainty of ±0.2 °C.

In order to calculate the mass diffusion coefficient from the interference fringe image, the primary goal is to establish the relationship between the mass diffusion coefficient and the phase of the object wave. Along with the development of the mass diffusion in the experiment, the refractive index of the solution changes continuously and the phase of the object wave changes concomitantly. And it leads to a continuous change of the interference fringe on the hologram. So if we extract the phase of the object wave from the interference fringe image and utilize the relationship between the mass diffusion coefficient and the phase of the object wave, the mass diffusion coefficient can be obtained.

For one-dimensional mass diffusion, the mass diffusion coefficient D_{AB} can be expressed as the following equation which was deduced from the second Fick's law [13]:

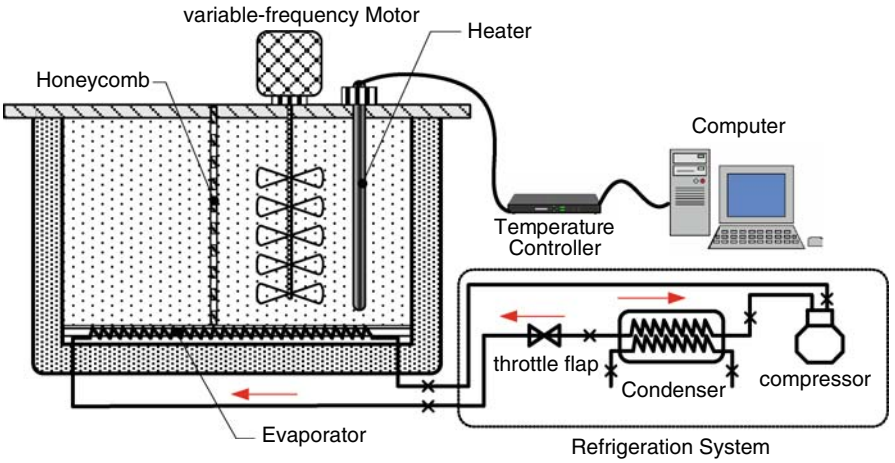

Fig. 3 Circulating water bath thermostatic system

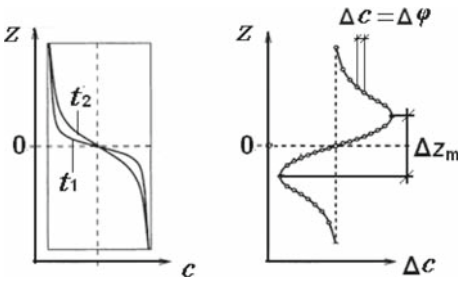

Fig. 4 Distributions of concentration and it's change

$$D_{AB} = \Delta z_m^2 \frac{t_1/t_2 - 1}{8t_1 \ln(t_1/t_2)} \tag{1}$$

where t_1 and t_2 are the moments of collecting the interference fringes and Δz_m is the vertical distance between the two extreme points of the solution's concentration difference, as shown in Fig. 4.

From Eq. 1, we can see that so long as t_1, t_2, and Δz_m are obtained, the mass diffusion coefficient can be calculated. t_1 and t_2 may be read from the computer timer, and Δz_m may be extracted from the phase information of the object wave. The relationship between the phase change of the object wave and the change of concentration is

$$\Delta\varphi = k\frac{\Delta c l 2\pi}{\lambda} \tag{2}$$

where $\Delta\varphi$ is the phase difference of two object waves at different times, Δc is the concentration difference of solution, k is the ratio coefficient pertinent with the solution's refractive index, λ is the wavelength of the laser beam, and l is the width of the diffusion cell in the direction of the laser beam.

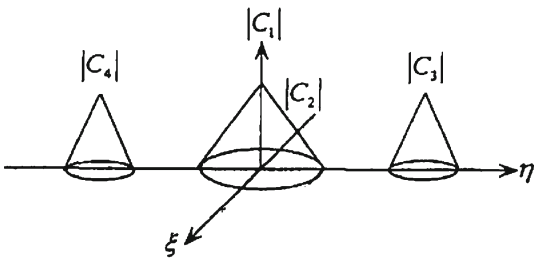

Fig. 5 Frequency spectrum of the interference fringe

From Eq. 2, we can see that the relationship between the phase difference of the object wave and the difference of concentration is linear, so the vertical distance between the two extreme points of concentration difference is equal to that of the object wave's phase. Therefore, to calculate the mass diffusion coefficient is to determine $\Delta\varphi$. The method of Fourier transformation phase measurement is used to determine this value in our study.

The complex amplitudes of the object wave $O(x, y)$ and reference wave $R(x, y)$ can be represented as

$$O(x, y) = o(x, y) \exp[-i\varphi(x, y)] \tag{3}$$

$$R(x, y) = r(x, y) \exp[-i\varphi'(x, y)] \tag{4}$$

The object wave and reference wave interfere to form the interference fringe hologram, and its intensity distribution is

$$\begin{aligned} I(x, y) = |R(x, y) + O(x, y)|^2 &= |R(x, y)|^2 + |O(x, y)|^2 + R^*(x, y)O(x, y) \\ &+ O^*(x, y)R(x, y) = |R(x, y)|^2 + |O(x, y)|^2 \\ &+2r(x, y)o(x, y) \cos\left[\varphi(x, y) - \varphi'(x, y)\right] \end{aligned} \tag{5}$$

From the Fourier transformation of the interference fringe hologram, the frequency spectrum of the interference fringe may be obtained as (see Fig. 5)

$$G(\xi, \eta) = C_1(\xi, \eta) + C_2(\xi, \eta) + C_3(\xi, \eta) + C_4(\xi, \eta) \tag{6}$$

where C_1 represents the frequency spectrum of the reference wave, C_2 represents the self-correlation part and the cross-correlation part of the object wave, C_3 represents the frequency spectrum of the original object wave, and C_4 represents the frequency spectrum of the conjugate image of the object wave.

By removing C_1, C_2, and C_4 on the frequency spectrum of the interference fringe with a rectangular window filter, we can obtain the frequency spectrum of the original object wave C_3. Then, performing an inverse Fourier transformation to transform C_3 to the spatial domain, the original object wave can be obtained. From two object waves of different moments, the wrapped phase difference $\Delta\psi$ can be calculated. Unwrapping the wrapped phase difference, the distribution of continual phase difference $\Delta\varphi$

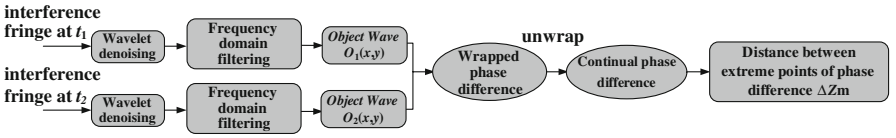

Fig. 6 Image processing based on Fourier transformation phase examination

can be obtained, from which we can read the distance between the two extreme points Δz_{m}. Finally, inserting Δz_{m}, t_1, and t_2 into Eq. 1, the mass diffusion coefficient D_{AB} can be obtained.

3 Image Processing Method

The processing method of holographic interference fringe images used in this study mainly includes the following steps, as shown in Fig. 6.

Taking the interference fringe image of a liquid–liquid mass diffusion system as an example, the entire process of the image processing method is introduced below.

3.1 Image Gathering and Wavelet De-noising

The interference fringe image was collected and transmitted to the computer by a CCD camera, and was recorded as a digital matrix by MATLAB, the value of each pixel on the interference fringe image represents the intensity of laser light.

In the process of gathering the interference fringe image, there are many factors that lead to the existence of errors on the interference fringe image, such as the uncorrelated light, the dust in the path of the light, the water fog on the glass wall of the diffusion cell, etc. So the reduction of noise is necessary for further processing of the interference fringe image. Considering that the phase information of the object wave exists in the details of the interference fringe image, the traditional de-noising methods such as the mean-value filter and the mid-value filter are not appropriate here. The wavelet de-noising technique is a multi-scale frequency analyzing method, and it can reduce the noise sufficiently and retain the useful information at the same time.

In this article, an improved wavelet de-noising method using the NeighCoeff method [14] with a 3×3 window $B_{i,j}$ to de-noise the interference fringe image is proposed. It includes the following steps: (1) decompose the interference fringe image to the wavelet domain with "db5" wavelet by five layers. (2) Accumulate all squares of the wavelet coefficients in the window $B_{i,j}$ in each frequency band, and compare the results with the squares of Donoho's universal threshold [15]. If the former is less than the latter, the wavelet coefficient is set to zero, or it will be shrunk by a factor of β. (3) Perform the inverse wavelet transformation and reconstruct the interference fringe image. The wavelet coefficient is determined by the following algorithmic equations:

$$d_{i,j} = \begin{cases} 0 & \sum_{B_{i,j}} {d_{i,j}}^2 < \lambda^2 \\ d_{i,j} \times \beta_{i,j} & \sum_{B_{i,j}} d_{i,j}^2 > \lambda^2 \end{cases} \tag{7}$$

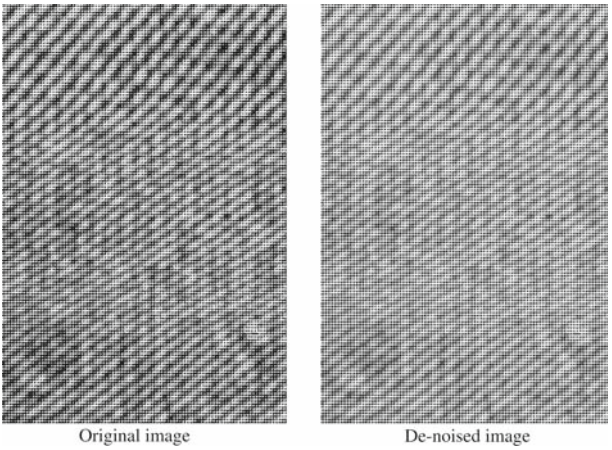

Fig. 7 (**a**) Original interference fringe image and (**b**) de-noised interference fringe image

$$\lambda = \sigma\sqrt{2\log mn} \quad \beta_{i,j}\left(1 - \lambda^2 \Big/ \sum_{B_{i,j}} d_{i,j}^2\right)$$

where d is the wavelet coefficient, λ is Donoho's universal threshold, β is the shrink factor of the wavelet coefficient, and m, n are the dimensions of the interference fringe image. The de-noising result is shown in Fig. 7, and we can see that the de-noising result is very effective.

3.2 Frequency-Domain Filtering and Reconstruction of Object Wave

The process of frequency-domain filtering used in this study is shown in Fig. 8. $H(\zeta, \eta)$ is the transfer function of the rectangular window filter, its usage is to preserve the frequency component of the object wave and remove other irrelevant frequency components.

After performing a two-dimensional Fourier transform to the de-noised interference fringe image, the frequency spectrum (see Fig. 9a) of the interference fringe image can be obtained. Then the frequency spectrum is filtered with a rectangular window to

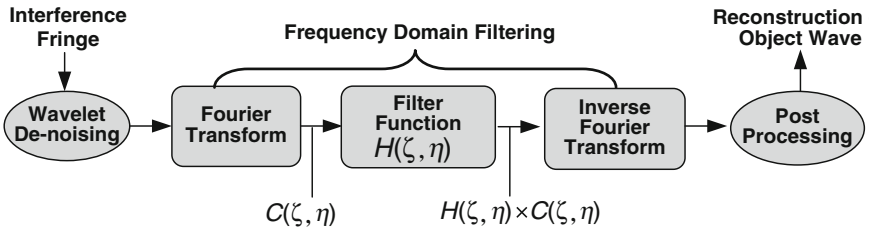

Fig. 8 Steps of frequency domain filtering

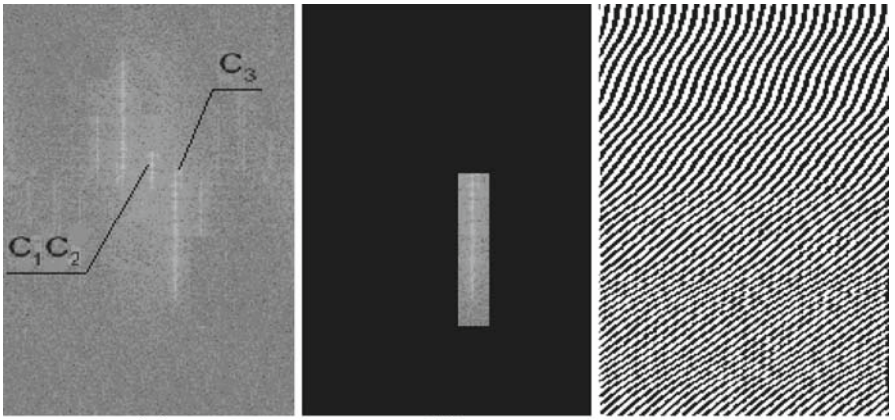

Fig. 9 Frequency spectrum and reconstruction of object wave: (**a**) frequency spectrum of interference fringe image, (**b**) first-level frequency spectrum extracted by a rectangular window, (**c**) reconstruction of the object wave

extract the first-level frequency spectrum (see Fig. 9b), which contains the information of the object wave. The inverse Fourier transform was performed to reconstruct the object wave (see Fig. 9c) in the spatial domain, as shown in Fig. 9.

Figure 10 shows the filtering results by the method of a Butterworth band-pass filter, Gauss band-pass filter, and rectangular window filter. Figure 11 shows the comparison of the reconstructed object wave by three different filter methods. From Fig. 10, we can see that the problem of the conventional filter method is filtering insufficiently or overly and this will lead to the inaccuracy of the reconstructed object wave such as the indistinctness and rupture (as shown in Fig. 11a, b). Compared with the first two filter methods, the rectangular window filter method is more effective, and it can extract the first level of the frequency spectrum more precisely. The rectangular window sufficiently preserved the useful frequency component and thoroughly removed the other unrelated frequency components. The reconstructed object wave is distinct and has no rupture (as shown in Fig. 11c), and it establishes a good foundation for subsequent image processing.

3.3 Determinations of Phase Difference and Δz_{m}

Finding the ratio of the reconstructed object waves of different moments $O_2(x, y)$ and $O_1(x, y)$

$$Q(x, y) = \frac{O_2(x, y)}{O_1(x, y)} = \exp\{j[\psi_2(x, y) - \psi_1(x, y)]\} = \exp[j\Delta\psi(x, y)] \quad (8)$$

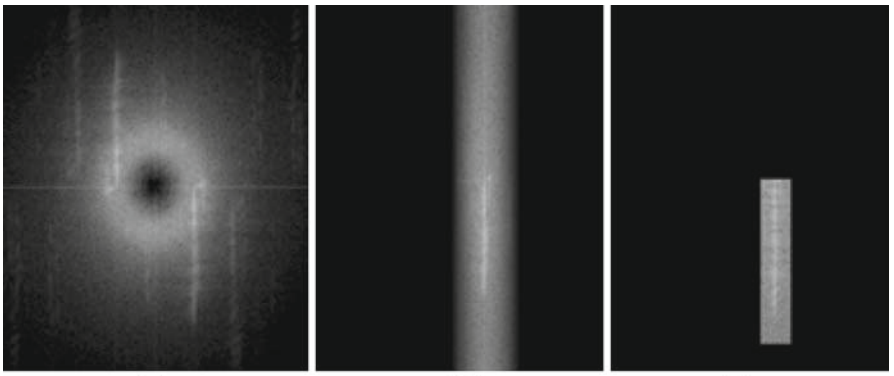

Fig. 10 The comparison of the frequency-domain filter by different methods: (**a**) filtering results with Butterworth band-pass filter, (**b**) filtering results with Gauss band-pass filter, (**c**) filtering results with rectangular window filter

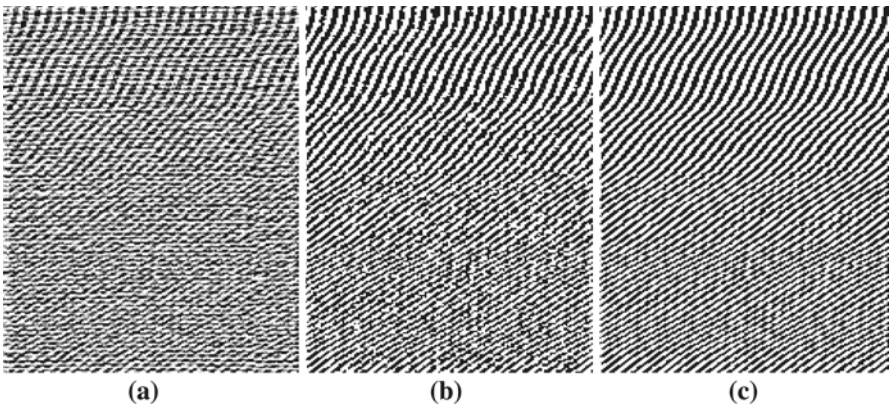

Fig. 11 The comparison of the reconstructed object wave by different filter methods: (**a**) reconstructed object wave with Butterworth band-pass filter, (**b**) reconstructed object wave with Gauss band-pass filter, (**c**) reconstructed object wave with rectangular window filter

Using the following logarithm algorithm to compute the wrapped phase difference of two reconstructed object waves, its distribution is obtained, as shown in Fig. 12a.

$$\log[Q(x, y)] = j\Delta\psi(x, y) \tag{9}$$

The value obtained after the above operation is merely the wrapped phase difference $\Delta\psi(x, y)$, and it is wrapped in $[-\pi \sim \pi]$. In order to obtain the continuous phase difference $\Delta\varphi(x, y)$, the unwrapping operation to the wrapped phase difference $\Delta\psi(x, y)$ is performed.

Considering both the practicability and the algorithmic efficiency, a least-squares phase unwrapping method to unwrap the wrapped phase difference is adopted. For a two-dimensional wrapped phase image, the relationship between the wrapped phase

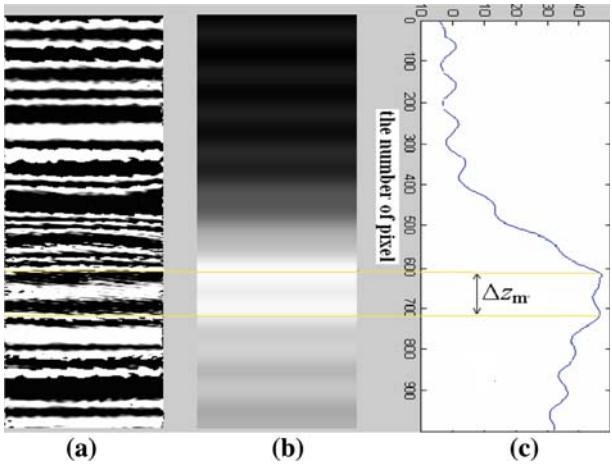

Fig. 12 Phase difference of object waves: (**a**) distribution of wrapped phase difference $\Delta\psi(x, y)$, (**b**) distribution of continual phase difference $\Delta\varphi(x, y)$, (**c**) linear distribution of continual phase difference

$\Delta\psi(x, y)$ and the continuous phase $\Delta\varphi(x, y)$ is $\Delta\varphi(x, y) = \Delta\psi(x, y) + 2K\pi$ $(K = 0, 1, 2, \ldots)$.

The primary goal of the least-squares unwrapping method is to calculate the result of the following formula:

$$\min\left\{\sum_{x,y}|\nabla_x\varphi(x, y) - W[\nabla_x\psi(x, y)]|^2 + \sum_{x,y}\left|\nabla_y\varphi(x, y) - W[\nabla_y\psi(x, y)]\right|^2\right\}$$

where W is the wrap function $W[\varphi(i, j)] = \psi(i, j)$

To calculate the minimum of the above formula is equivalent to solving the discrete Poisson equation,

$$\begin{aligned}&[\varphi(x + 1, y) - 2\varphi(x, y) + \varphi(x - 1, y)]\\ &\quad + [\varphi(x, y + 1) - 2\varphi(x, y) + \varphi(x, y - 1)] = \rho(x, y)\end{aligned} \tag{10}$$

In the above equation,

$$\begin{aligned}\rho(x, y) = {} & W[\nabla_x\psi(x, y)] - W[\nabla_x\psi(x - 1, y)] + W[\nabla_y\psi(x, y)]\\ & - W[\nabla_y\psi(x, y - 1)]\end{aligned} \tag{11}$$

From Eqs. 10 and 11, the continual phase difference $\Delta\varphi(x, y)$ (Fig. 12b) can be calculated from $\Delta\psi(x, y)$.

Through calculating the mean value of each row vector of the continual phase difference matrix, the line of continual phase difference is obtained, as shown in Fig. 12c. The y-coordinate represents for the number of pixels, and the value of Δz_m can be determined from it.

4 Experimental Verification and Uncertainty Analysis

In order to verify the accuracy and reliability of the image processing method, mass diffusion coefficients of saccharose in an aqueous solution at condensation of $0.1\,\mathrm{mol}\cdot\mathrm{L}^{-1}$ were measured at five different temperatures, the interference images were gathered and processed using the new method and a least-squares fit of the centerline of interference fringes. Comparison of experimental results in this study and literature data are presented in Table 1 and Fig. 13.

From Table 1 and Fig. 13, we can see that the image processing method used in this study can improve the data processing accuracy greatly. Compared with literature data, the relative deviation of mass diffusion coefficients of saccharose in aqueous solution obtained with the image processing method of this study can be controlled within 3 %, while the relative deviation obtained with the previous method is about 5 %. The previous method uses only an integral gray grade, by comparison, the method introduced

Table 1 Experimental results for different processing methods

T (K)	Reference data [16] $10^6 D_{AB}$ ($cm^2 \cdot s^{-1}$)	This study $10^6 D_{AB}$ ($cm^2 \cdot s^{-1}$)	R.D.[a] σ_1 (%)	The previous method[b] $10^6 D_{AB}$ ($cm^2 \cdot s^{-1}$)	R.D.[a] σ_1 (%)
288.15	4.62	4.67	1.08	4.72	2.22
298.15	5.56	5.64	1.44	5.69	2.35
303.15	5.89	5.98	1.53	6.06	2.86
313.15	7.66	7.81	1.96	8.02	4.57
333.15	9.87	10.11	2.43	10.37	4.84

[a]Relative deviation,
[b]Processing method of least-squares fit of centerline of interference fringe

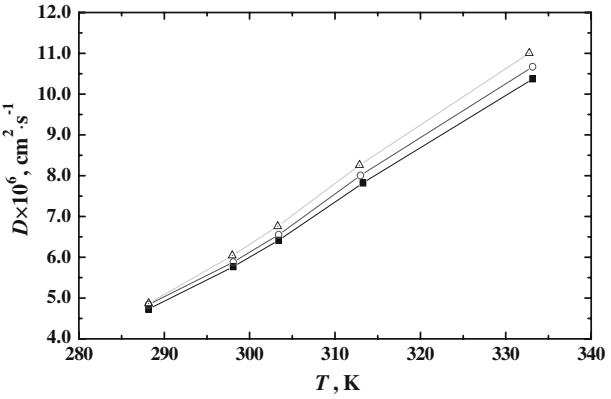

Fig. 13 Mass diffusion coefficients of saccharine in aqueous solution: -■- literature data, -○- experimental data in this study, -△- experimental data obtained by the method of least square fitting of the centerline of interference fringe

in this study use all the gray scale information, so the data processing accuracy is improved greatly.

To determine the experimental uncertainty in the measurement, the following equation is used [17]:

$$U = ku_c = k\sqrt{\sum (u_i)^2} \tag{12}$$

where subscript i is the influencing factor of the mass diffusion coefficient, u_i is the uncertainty for each variable, u_c is the compound uncertainty for each variable, and k is the confidence coefficient (it is usually taken to be 2 or 3). When $k = 2$, the degree of confidence is 95 %; When $k = 3$, the degree of confidence is 99 %. In this study, the confidence coefficient of the compound uncertainty is taken to be 2.

The experimental method of measuring the mass diffusion coefficient used in this study is laser holographic interferometry, it is an indirect measuring technique. We need to measure t_1, t_2, and Δz_m, and insert them into Eq. 1 to compute the mass diffusion coefficient; therefore, the experimental uncertainty was determined in measuring these three physical quantities.

t_1 and t_2 were recorded automatically by software developed by VC++, and its uncertainty was estimated to be 10^{-3} s; therefore, the absolute uncertainty in dt_1 and dt_2 is 10^{-3} s. Considering the elapsed time between t_1 and t_2, the uncertainty in time is 2.22 ppm.

In the entire process of image processing, the largest uncertainty which influences the final result for Δz_m was produced in the step of unwinding the wrapped phase difference, the uncertainty of this step reaches several pixels, which is 10^{-5} m in magnitude. Therefore, the absolute uncertainty of the final result Δz_m is 10^{-5} m. Considering the size of the interference fringe, the uncertainty in Δz_m is 0.1 %.

The experimental uncertainties in temperature and mass diffusion coefficient in this study are estimated to be no greater than 0.16 K and 0.2 %, respectively, as shown in Table 2.

Table 2 Experimental uncertainty of temperature and mass diffusion coefficient

Temperature	
Platinum resistance thermometer, u_1 (K)	0.01
Data collection and process detector equipment, u_2 (K)	0.025
Temperature control system, $u_3(K)$	0.05
Temperature stability of constant temperature cabinet, $u_4(K)$	0.05
Combined standard uncertainty, u_c (K)	0.08
Mass diffusion coefficient	
Time of determining hologram, u_1 (ppm)	2.22
Distance between two extreme points of concentration, u_2 (%)	0.1
Combined standard uncertainty, u_c (%)	0.1

Table 3 Mass diffusion coefficients of ethylene glycol dimethyl ether (GDME) and diethylene glycol dimethyl ether (DGM) in air

T (K)	GDME (1) + Air (2)		DGM (1) + Air (2)	
	$10^5 D_{AB}$ ($cm^2 \cdot s^{-1}$)	$10^5 u_{D_{12}}$ ($cm^2 \cdot s^{-1}$)	$10^5 D_{AB}$ ($cm^2 \cdot s^{-1}$)	$10^5 u_{D_{12}}$ ($cm^2 \cdot s^{-1}$)
278.15	7.680	±0.0021	6.228	±0.0022
281.15	7.733	±0.0024	6.284	±0.0022
284.15	7.783	±0.0023	6.326	±0.0021
287.15	7.862	±0.0022	6.391	±0.0022
290.15	7.938	±0.0022	6.439	±0.0023
293.15	8.026	±0.0024	6.488	±0.0022
296.15	8.132	±0.0021	6.565	±0.0021
299.15	8.266	±0.0022	6.638	±0.0021
302.15	8.399	±0.0021	6.717	±0.0022
305.15	8.526	±0.0022	6.820	±0.0022
308.15	8.680	±0.0021	6.933	±0.0021
311.15	8.851	±0.0020	7.059	±0.0022
314.15	9.020	±0.0022	7.185	±0.0024
317.15	9.181	±0.0021	7.329	±0.0025
320.15	9.384	±0.0023	7.498	±0.0024
323.15	9.586	±0.0022	7.638	±0.0024
326.15	9.829	±0.0023	7.787	±0.0023
329.15	10.06	±0.0024	7.961	±0.0023
332.15	10.29	±0.0023	8.174	±0.0022
335.15	10.56	±0.0021	8.387	±0.0024
338.15	10.82	±0.0022	8.629	±0.0023

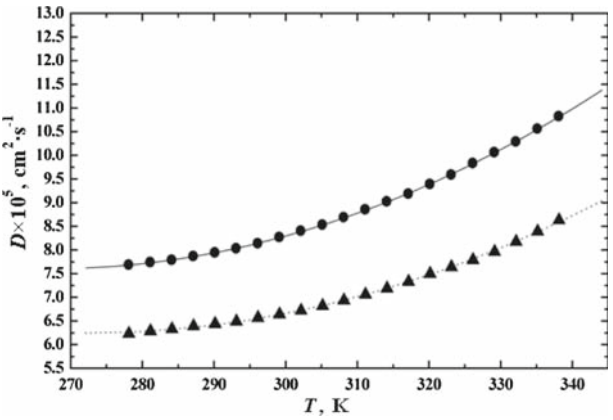

Fig. 14 Mass diffusion coefficients of ethylene glycol dimethyl ether (GDME) and diethylene glycol dimethyl ether (DGM) in air. • experimental data of GDME, — polynomial fit of experimental data of GDME, ▲ experimental data of DGM, ... polynomial fit of experimental data of DGM

5 Mass Diffusion Coefficients of Some Fuel Additives

With the method introduced above, mass diffusion coefficients of two fuel additives, ethylene glycol dimethyl ether and diethylene glycol dimethyl ether in air were measured from 278.15 K to 338.15 K.

The experimental results of the mass diffusion coefficients of ethylene glycol dimethyl ether (GDME) and diethylene glycol dimethyl ether (DGM) in air at $T = (278.15 \text{ to } 338.15)$ K are reported in Table 3 and Fig. 14. A polynomial for calculating the mass diffusion coefficients of ethylene glycol dimethyl ether in air was fitted to the experimental data at $T = (278.15 \text{ to } 338.15)$ K, as follows:

$$D_{\mathrm{AB}} = 1.243 \times 10^{-3} - 1.245 \times 10^{-5} T + 4.298 \times 10^{-8} T^2 - 4.751 \times 10^{-11} T^3 \tag{13}$$

The polynomial of calculating the mass diffusion coefficients ethylene glycol dimethyl ether in air was fitted by the experimental data at $T = (278.15 \text{ to } 338.15)$ K, as following:

$$D_{\mathrm{AB}} = 1.241 \times 10^{-3} - 1.223 \times 10^{-5} + 4.125 \times 10^{-8} T^2 - 4.484 \times 10^{-11} T^3 \tag{14}$$

6 Conclusions

A new method of processing Mach–Zehnder interference fringe images is introduced in this article. The method makes use of phase information of interference fringe images to calculate the mass diffusion coefficient and significantly improved the data processing precision when compared with traditional methods. By an experimental uncertainty analysis and experimental verification, the reliability of the new method is demonstrated. The experimental uncertainty in temperature and in the mass diffusion coefficient is estimated to be 0.16 K and 0.2 % respectively. On this basis, the mass diffusion coefficients of two fuel additives, ethylene glycol dimethyl ether and diethylene glycol dimethyl ether in air within the temperature range from 279 K to 335 K were measured.

Acknowledgments This study was supported by the National Nature Science Fund Committee (NSFC No. 50676069) and NSFC Fund for Creative Research Groups (No.50521604). The authors gratefully acknowledge them for financial support of this study.

References

1. G.S. Spagnolo, D. Ambrosini, A. Ponticiello, D. Paoletti, J. Phys. III France **6**, 1117 (1996)
2. A. Anand, V.K. Chhaniwal, S. Mukherjee, C.S. Narayanamurthy, Opt. Laser Technol. **34**, 45 (2002)
3. V.K. Chhaniwal, A. Anand, S. Girhe, D. Patil, N. Subrahmanyam, C.S. Narayanamurthy, J. Opt. A: Pure Appl. Opt. (Special Edition) **5**, S329 (2003)
4. G. Ying, H. Maogang, Z. Qiu, Z. Ying, Energy **34**, 1560 (2009)
5. E. Ruckenstein, L. Hongqin, Ind. Eng. Chem. Res. **36**, 3927 (1997)
6. G.M. Grass, S.A. Sweetana, Pharmaceut. Res. **5**, 372 (1988)

7. N. Matsunaqa, M. Hori, Heat Transf. Asian Res. **31**, 182 (2002)
8. V. Botton, P. Lehmann, Int. J. Heat Mass Transf. **44**, 3345 (2001)
9. T.O. Hushcha, A.I. Luik, Talanta **53**, 29 (2000)
10. L. Gabelmann-Gray, H. Fenichel, Appl. Opt. **18**, 343 (1979)
11. C. Mattisson, T. Nylander, A. Axelsson, G. Zacchi, Chem. Phys. Lipids **84**, 1 (1996)
12. M.G. He, Q. zhong, Y. Zhang, High Temp.-High Press. **37**, 61 (2008)
13. G. Ying, H. Maogang, Z. Qiu, Z. Ying, J. Chem. Eng. Data **53**, 2861 (2008)
14. G.Y. Chen, T.D. Bui, A. Krzyzak, Integr. Comp.-Aided Eng. **12**, 99 (2005)
15. D.L. Donoho, IEEE Trans. Inf. Theory **41**, 613 (1995)
16. L.G. Gray, H. Fenichel, Appl. Opt. **18**, 343 (1979)
17. BIPM, IEC, IFCC, ISO, IUPAC, IUPAP, OIML, *Guide to the Expression of Uncertainty in Measurement* (International Organization for Standardization, Genevese, 1995), pp. 116–134 (corrected and reprinted)